*Remote Sens.* **2015**, *7*, 7080-7104; doi:10.3390/rs70607080

OPEN ACCESS

*remote sensing*

**ISSN 2072-4292**

www.mdpi.com/journal/remotesensing

*Article*

# Evaluation of Land Surface Temperature Retrieval from FY-3B/VIRR Data in an Arid Area of Northwestern China

**Jinxiong Jiang [1,2,3], Hua Li [1,2,*], Qinhuo Liu [1,2,*], Heshun Wang [1], Yongming Du [1], Biao Cao [1], Bo Zhong [1] and Shanlong Wu [1]**

[1] State Key Laboratory of Remote Sensing Science, Institute of Remote Sensing and Digital Earth, Chinese Academy of Sciences, Beijing 100101, China; E-Mails: xiongxiong2008_0@163.com (J.J.); heshun8336@163.com (H.W.); duym@radi.ac.cn (Y.D.); caobiao@radi.ac.cn (B.C.); zhongbo@radi.ac.cn (B.Z.); wsl0579@163.com (S.W.)

[2] Joint Center for Global Change Studies (JCGCS), Beijing 100875, China

[3] College of Resources and Environment, University of Chinese Academy of Sciences, Beijing 100049, China

* Authors to whom correspondence should be addressed; E-Mails: lihua@radi.ac.cn (H.L.); liuqh@radi.ac.cn (Q.L.); Tel./Fax: +86-010-6480-6256 (H.L.); +86-010-6484-9840 (Q.L.).

Academic Editors: Xin Li, Yuei-An Liou, Richard Müller and Prasad S. Thenkabail

*Received: 10 March 2015 / Accepted: 13 May 2015 / Published: 29 May 2015*

---

**Abstract:** This paper uses the refined Generalized Split-Window (GSW) algorithm to derive the land surface temperature (LST) from the data acquired by the Visible and Infrared Radiometer on FengYun 3B (FY-3B/VIRR). The coefficients in the GSW algorithm corresponding to a series of overlapping ranges for the mean emissivity, the atmospheric Water Vapor Content (WVC), and the LST are derived using a statistical regression method from the numerical values simulated with an accurate atmospheric radiative transfer model MODTRAN 4 over a wide range of atmospheric and surface conditions. The GSW algorithm is applied to retrieve LST from FY-3B/VIRR data in an arid area in northwestern China. Three emissivity databases are used to evaluate the accuracy of different emissivity databases for LST retrieval, including the ASTER Global Emissivity Database (ASTER_GED) at a 1-km spatial resolution (AG1km), an average of twelve ASTER emissivity data in the 2012 summer and emissivity spectra extracted from spectral libraries. The LSTs retrieved from the three emissivity databases are evaluated with ground-measured LST at four barren surface sites from June 2012 to December 2013 collected during the HiWATER field campaign. The results indicate that using emissivity

extracted from ASTER_GED can achieve the highest accuracy with an average bias of 1.26 and −0.04 K and an average root mean square error (RMSE) of 2.69 and 1.38 K for the four sites during daytime and nighttime, respectively. This result indicates that ASTER_GED is a useful emissivity database for generating global LST products from different thermal infrared data and that using FY-3B/VIRR data can produce reliable LST products for other research areas.

**Keywords:** land surface temperature; FY-3B/VIRR; Generalized Split-Window; land surface emissivity; ASTER_GED; ground-measured LST

## 1. Introduction

As one of the key parameters in land-surface process physics and a result of surface-atmosphere interactions at local and global scales, land surface temperature (LST) is important to climatology, meteorology, hydrology, ecology, and a wide range of interdisciplinary research areas [1–10]. Satellite remote sensing is the only possible way for measuring LST at a high spatial resolution and temporal frequency [11] due to the strong spatial heterogeneity in land surface characteristics, such as vegetation, topography and soil physical properties [11–13]. Using satellite infrared imagery to estimate LST has been a research focus since 1975. Although many algorithms and methods have been proposed to retrieve LST, highly accurate LST products have been difficult to obtain at the global scale [11]. According to [14], satellite-derived LST products with an accuracy of 0.3 K for ocean and 1 K for the land surface are required. Hence, improving the accuracy of satellite-derived LST is critical. Comprehensive reviews have summarized the algorithms for retrieving LST from satellite images [11,15,16]. These methods are grouped roughly into two major categories in Li *et al.* [11] according to whether the land surface emissivity (LSE) was used as *a priori* information. The single-channel, multi-channel, and multi-angle methods belong to the first category (*i.e.*, LSE is known and used as a priori information in these algorithms), while the stepwise retrieval method, simultaneous retrieval of LSEs and LST with known atmospheric information, and simultaneous retrieval with unknown atmospheric information belong to the second category. The split-window (SW) algorithm is a multi-channel method and is based on the fact that the difference of the atmospheric water vapor absorptions at selected longwave infrared channels is proportional to the difference in the brightness temperature (BT) at two channels [17]. Due to its simplicity and robustness, the SW algorithm has been applied widely to various satellite data, such as the Advanced Very High Resolution Radiometer (AVHRR) [18–20], Moderate Resolution Imaging Spectroradiometer (MODIS) [14,21,22], LandSat-8 [23,24], FengYun polar-orbiting meteorological satellite (VIRR/FY-3A) data [25–27], Spinning Enhanced Visible and Infrared Imager (SEVIRI) [28–30], Advanced Along-Track Scanning Radiometer (AATSR) [31], Geostationary Operational Environmental Satellites (GOES) [32], FengYun geostationary meteorological satellite (FY-2C) [33], and others.

The second generation of the Chinese polar-orbiting meteorological satellite, FengYun 3B (FY-3B), is an afternoon orbiting satellite and was launched on 5 November 2010. The Visible and Infrared Radiometer (VIRR) sensor carried on FY-3B provides observations of two thermal infrared spectral

bands (TIR 4: 10.3–11.3 μm and TIR 5: 11.5–12.5 μm) with a spatial resolution of 1 km, which are consistent with the two thermal bands (TIR bands 31 and 32) of MODIS. Several studies in the last few years have indicated that the generalized split-window (GSW) algorithm [14] and the subsequently refined GSW algorithm [21,22] work well in retrieving LST from MODIS TIR bands 31 and 32 [34–36]. Several SW formulas similar to the GSW algorithm are proposed to estimate LST from China's meteorological satellite [25,26,33 and obtained reliable results. For example, Tang *et al.* [33] used the GSW algorithm to estimate LST from FY-2C data, Jiang *et al.* [26] adopted the GSW algorithm to estimate LST from FY-3A/VIRR data. However, a limitation of those studies is a lack of algorithm validation with *in situ* LST measurements. Validation of LST products generated from different satellite data not only provides LST users with product quality information, but also identifies possible deficiencies and further improves the LST retrieval algorithms. Thus, more LST product validations are needed, especially for Chinese satellite data.

The aims of this paper are to use the refined GSW algorithm [21] to estimate LST from FY-3B/VIRR data and to evaluate the results with long-term ground-measured LST for four barren surface sites collected during the Heihe Watershed Allied Telemetry Experimental Research (HiWATER) field campaign [37,38]. Previous studies [37,39] indicated that the split-window algorithms generally underestimate the LST over very warm arid regions, especially barren surfaces. The barren surface emissivity values used in the split-window algorithm are constants and only depend on surface type. However, the emissivity change caused by natural variation, such as vegetation and soil physical properties, was not considered within each surface type, which may explain the underestimation in LST. Using maps of surface emissivity physically retrieved from satellite data (like those from ASTER-TES, MODISMOD11B1 or MOD21 products) may address this issue. In this paper, three emissivity databases are used to evaluate the accuracy of different emissivity databases for LST retrieval, including the ASTER Global Emissivity Database (ASTER_GED) at a 1-km spatial resolution (AG1km), an average of twelve ASTER emissivity data in the 2012 summer and emissivity spectra extracted from spectral libraries. The framework of this paper includes four sections. Section 2 describes the refined GSW algorithm, how to obtain the coefficients in the GSW algorithm, and sensitivity analyses. The LST results and evaluation for four sites are presented in Section 3. Finally, Section 4 concludes this paper.

## 2. Methodology

### *2.1. The GSW Algorithm for FY-3B/VIRR*

Due to less sensitivity to the uncertainties in the LSEs and the atmospheric conditions, the GSW algorithm has been applied widely to various new generation satellite data to retrieve LST and obtained reliable results [25–30,32]. Wan [21] proposed a refined GSW algorithm to improve the LST accuracy and it is directly applied to the FY-3B/VIRR data to retrieve LST in this paper. The brightness temperatures of FY-3B/VIRR thermal bands four and five (*i.e.*, $T_4$ and $T_5$) in Equation (1) are used in this algorithm to estimate surface temperature $T_s$. A quadratic term representing the difference between the brightness temperatures of bands four and five (*i.e.*, $\Delta T = T_4 - T_5$) based on the original GSW formula is added to the refined formula to improve the LST accuracy. The quadratic term in the split-window algorithm can be traced back to Coll and Caselles [40].

$$T_s = C + (A_1 + A_2\frac{1-\varepsilon}{\varepsilon} + A_3\frac{\Delta\varepsilon}{\varepsilon^2})\frac{T_{45}}{2} + (B_1 + B_2\frac{1-\varepsilon}{\varepsilon} + B_3\frac{\Delta\varepsilon}{\varepsilon^2})\frac{\Delta T}{2} + D\Delta T^2 \quad (1)$$

where $\varepsilon = (\varepsilon_4 + \varepsilon_5)/2$, $\Delta\varepsilon = \varepsilon_4 - \varepsilon_5$, $T_{45} = T_4 + T_5$ and $\Delta T = T_4 - T_5$, and $\varepsilon_4$ and $\varepsilon_5$ are the emissivities of the FY-3B/VIRR thermal bands four and five, respectively; $A_1$, $A_2$, $A_3$, $B_1$, $B_2$, $B_3$, $C$, and $D$ are the algorithm coefficients.

### *2.2. Obtaining GSW Algorithm Coefficients*

The optimal coefficients (*i.e.*, $A_{1-3}$, $B_{1-3}$, $C$ and $D$) in Equation (1) are obtained in three steps in this paper: (1) building a look-up table (LUT) of the three atmospheric terms in an approximate radiative transfer expression (Equation (2)) under clear sky conditions [41], including the atmospheric transmittance, the atmospheric up-welling radiance, and the atmospheric down-welling radiance; (2) calculating the brightness temperatures at the top of the atmosphere (TOA) for FY-3B/VIRR bands four and five; and (3) building the LUT for the coefficients for the FY-3B/VIRR GSW algorithm based on different ranges of LST, emissivity, view zenith angles (VZAs) and water vapor content (WVC).

$$B_i(T_i) = \varepsilon_{i\theta}B_i(T_s)\tau_{i\theta} + L_{i\theta}^{atm\uparrow} + (1-\varepsilon_{i\theta})\tau_{i\theta}L_{ai}^{atm\downarrow} \quad (2)$$

where $\theta$ is the VZA, $\varepsilon_i$ is the surface emissivity for band $i$, $B_i(\ )$ is Planck's function for band $i$; $T_s$ is LST, $T_i$ is the TOA brightness temperature for band $i$, $\tau_{i\theta}$ is the atmosphere transmittance for band $i$ at VZA $\theta$, $L_{i\theta}^{atm\uparrow}$ is the atmospheric up-welling band radiance and $L_{ai}^{atm\downarrow}$ is the atmospheric down-welling band irradiance.

Step 1 used the MODTRAN (MODerate resolution atmospheric TRANsmission) 4.0 [42] and the TIGR-3 (Thermodynamic Initial Guess Retrieval database 3) atmospheric profiles [43] to simulate the atmospheric transmittance and up-welling/down-welling radiance under different conditions. TIGR3 is a climatological library of 2311 representative atmospheric situations selected by statistical methods from 80,000 radiosonde reports from polar to tropical atmospheres on a worldwide scale. Because the LST estimation is based on clear sky conditions, only 874 profiles are selected to establish the simulated database, in which the relative humidity at every level is less than 80%. The WVC of the selected profiles ranges from 0.05 to 6.27 g/cm$^2$, and the air temperature ($T_{air}$) in the first boundary layer of the 874 selected atmospheric profiles ranges from 231 to 315 K. The scatter plot between $T_{air}$ and the atmospheric WVC (Figure 1) indicates that the WVC is a function of $T_{air}$, and that 280 K is an inflection point. The atmospheric transmittance $\tau_{i\theta}$ and the atmospheric up-welling radiance $L_{i\theta}^{atm\uparrow}$ at 12 (0°, 10°, 20°, 30°, 40°, 50°, 56.05°, 59.84°, 62.84°, 65.27°, 67.29°, 69°) different VZAs and the atmospheric down-welling radiance at 53° [44] in Equation (2) are calculated in the 650–1252 cm$^{-1}$ spectral range at a 1-cm$^{-1}$ resolution using MODTRAN for extracted atmospheric profiles. Then, the results are convolved with the spectral response function of the FY-3B/VIRR bands four and five to obtain band-integrated atmospheric terms.

Equation (2) is used to calculate the TOA brightness temperature in step 2. The three atmospheric terms ($L_{i\theta}^{atm\uparrow}$, $L_{ai}^{atm\downarrow}$, $\tau_{i\theta}$) are obtained from the LUT in step 1. $T_s$ varies from $T_{air}$ − 16 to $T_{air}$ + 4 K for $T_{air} \leq 280$ K (cold atmosphere) and from $T_{air}$ − 5 to $T_{air}$ + 29 K for $T_{air} > 280$ K (warm atmosphere) in 1 K increments [21,45] to maximize algorithm performance over a wide range of conditions. $\varepsilon$ varies from 0.89 to 1 with a step of 0.01, and $\Delta\varepsilon$ varies from −0.037 to 0.027 with a step of 0.005. The TOA band radiance ($B_i(T_i)$) is converted to band brightness temperature using a built-in look-up table in steps of 0.1 K.

Finally, the coefficients in Equation (1) at 12 viewing angles are computed in two steps. First, a standard least squares regression is used to remove outliers with a 1.5-σ threshold. Second, a robust regression is used to compute the final coefficients with an iteratively reweighted least squares solution using a bi-square weighting function [46]. The averaged emissivity, WVC, LST are divided into several tractable sub-ranges to improve the fitting accuracy. The WVC is divided into six sub-ranges with an overlap of 0.5 g/cm$^2$: [0, 1.5], [1, 2.5], [2, 3.5], [3, 4.5], [4, 5.5], [5, 6.5]; ε is divided into two groups: [0.89, 0.96], [0.94, 1]. LST is divided into five sub-ranges with an overlap of 5 K: <280 K, [275, 295], [290, 310], [305, 325], and >320 K.

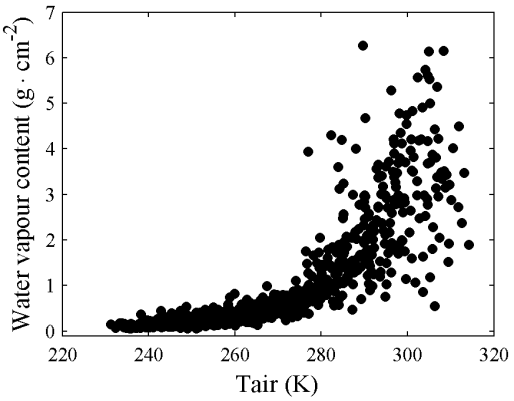


**Figure 1.** Scatter plots between $T_{air}$ and WVC of the selected 875 atmospheric profiles in the TIGR-3 database.

Figure 2 shows that the coefficients are a function of cosine of VZA (here WVC ϵ [1, 2.5] g/cm$^2$ and $T_s$ ϵ [290, 310] K). Similar results between these coefficients and the cosine of VZA are observed for other WVC and LST conditions. Therefore, the coefficients at other VZAs between 0° to 69° can be derived through polynomial curve fitting.

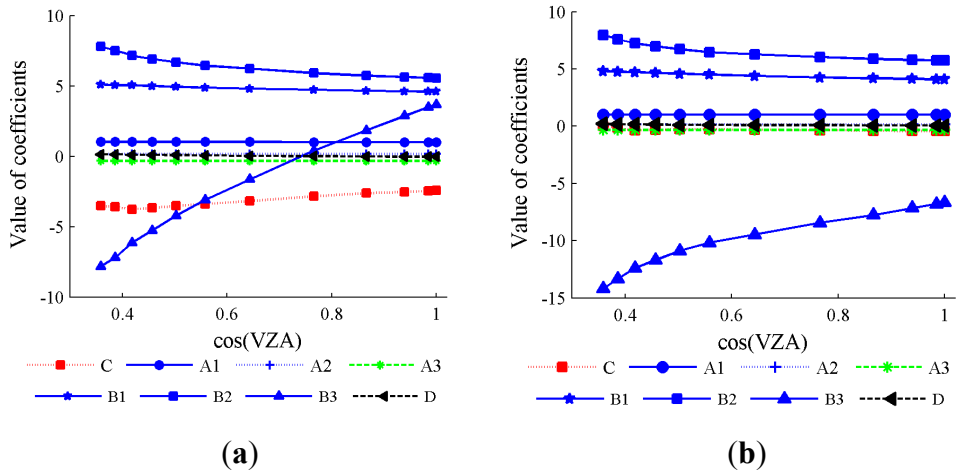


**Figure 2.** Examples of the GSW coefficients for VIRR/ FY-3B data with LST from 290 to 310 K and WVC from 1 to 2.5 g/cm$^2$ in two emissivity groups, respectively. (**a**) ε ϵ [0.89, 0.96], WVC ϵ [1, 2.5], LST ϵ [290, 310]; (**b**) ε ϵ [0.94, 1.00], WVC ϵ [1, 2.5], LST ϵ [290, 310].

Figure 3 shows the root mean square errors (RMSEs) between the estimated and actual $T_s$ as a function of the cosine of VZA for the two emissivity groups with different sub-ranges. It is worth noting that the RMSEs increase with VZA in all LST sub-ranges and rise sharply at larger VZA values (VZA > 60°), but the increase in RMSEs is small for drier atmospheres (*i.e.*, WVC < 2 g/cm$^2$). The RMSEs are less than 1.0 K for all sub-ranges when VZA ≤ 30° and WVC < 4.5 g/cm$^2$. Compared with the results for the entire LST range in Figure 3f, the RMSEs of others in Figure 3a–e are lower; thus, the fitting accuracy is improved.

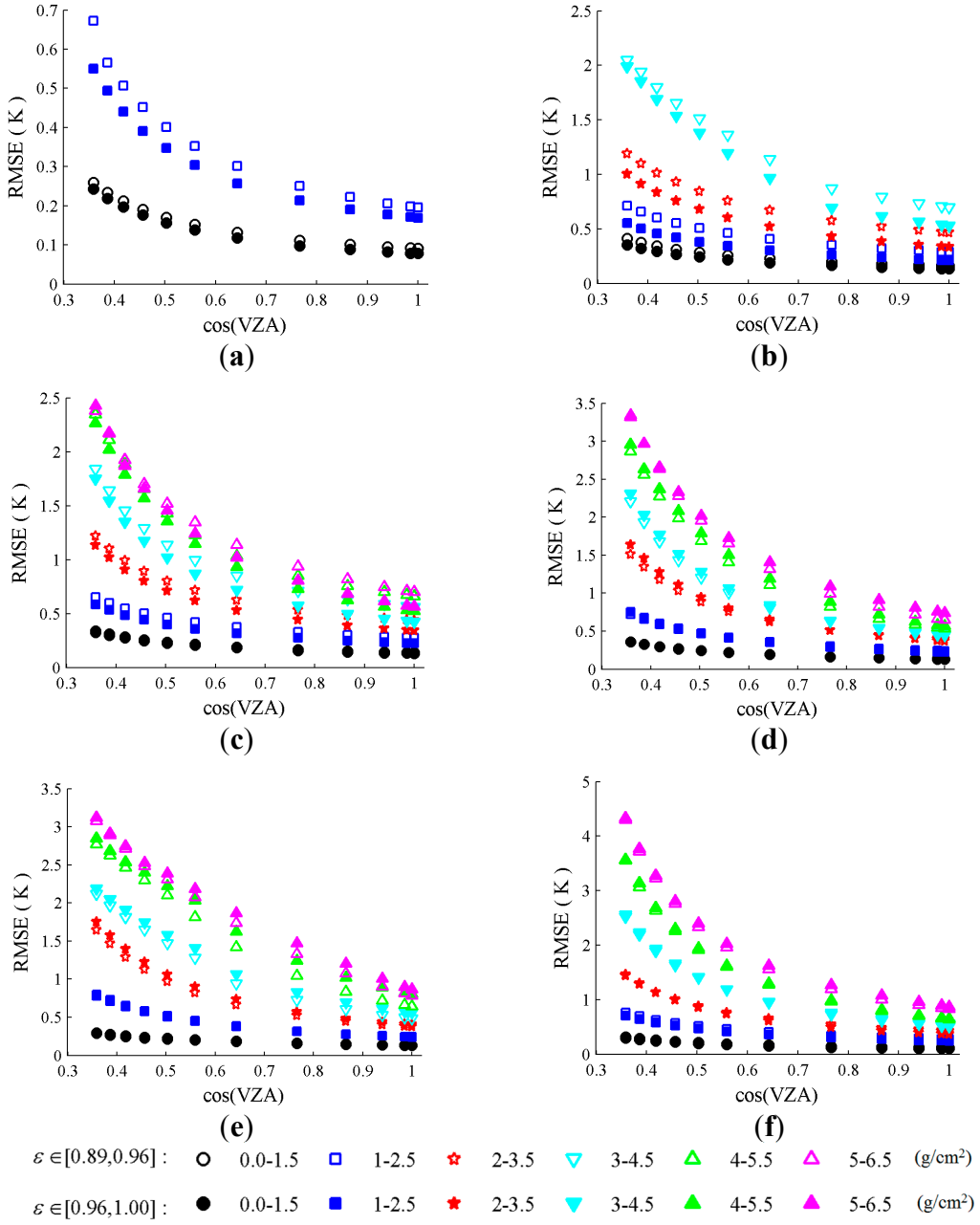


**Figure 3.** RMSEs between the estimated and actual $T_s$ as a function of the cosine of VZA for the two emissivity groups with different sub-ranges. (**a**) LST < 280 K; (**b**) 275 K < LST < 295 K; (**c**) 290 K < LST < 310 K; (**d**) 305 K < LST < 325 K; (**e**) 320 K < LST; (**f**) The whole LST range.

It should be noted that two steps should be executed when using the coefficients to estimate LST from actual satellite data. First, an approximate LST is computed using the coefficients from the GSW algorithms for the sub-range of LSE, WVC and the entire LST range at 12 VZAs. Then, a more accurate LST is determined according to the approximate LST obtained in the first step using coefficients within the sub-range of LSE, WVC, and LST. LSE and WVC as model input also are required when estimating LST from actual satellite data. The MODIS total precipitable water product MOD05 with a similar overpass time and the method proposed by Li *et al.* (2003) can be used to derive the atmospheric WVC [45]. When the input data (LSE or WVC) falls within the overlapping interval of two consecutive sub-ranges, the more near sub-range (from the central of the range) will be chosen.

### *2.3. Sensitivity Analysis*

An error analysis is performed to assess the sensitivity of the GSW algorithm. The theoretical error of this algorithm can be expressed as a Root Sum Square (RSS):

$$\begin{aligned}\delta(T_s) &= \sqrt{\delta(LST_1)^2 + \delta(LST_2)^2 + \delta(WVC)^2 + \delta(AD)^2} \\ &= \sqrt{\left[\alpha_{BT}{}^2\delta(T_{45})^2 + \beta_{BT}{}^2\delta(\Delta T)^2\right] + \left[\alpha^2\delta(\frac{1-\varepsilon}{\varepsilon})^2 + \beta^2\delta(\frac{\Delta\varepsilon}{\varepsilon^2})^2\right] + \delta(WVC)^2 + \delta(AD)^2}\end{aligned} \quad (3)$$

with:

$$\alpha_{BT} = 0.5(A_1 + A_2\frac{1-\varepsilon}{\varepsilon} + A_3\frac{\Delta\varepsilon}{\varepsilon^2}) \quad (3.1)$$

$$\beta_{BT} = 0.5(B_1 + B_2\frac{1-\varepsilon}{\varepsilon} + B_3\frac{\Delta\varepsilon}{\varepsilon^2}) + 2D(T_4 - T_5) \quad (3.2)$$

$$\alpha = A_2\frac{T_4 + T_5}{2} + B_2\frac{T_4 - T_5}{2} \quad (3.3)$$

$$\beta = A_3\frac{T_4 + T_5}{2} + B_3\frac{T_4 - T_5}{2} \quad (3.4)$$

where $\delta(T_s)$ is the RSS of the errors/uncertainties in LST, $\delta(LST_1)$, $\delta(LST_2)$, $\delta(WVC)$ and $\delta(AD)$ are LST errors caused by the uncertainty of the brightness temperature, the emissivity, WVC, and algorithm itself, respectively. $\delta(T_{45})$, $\delta(\Delta T)$, $\delta(\frac{1-\varepsilon}{\varepsilon})$ and $\delta(\frac{\Delta\varepsilon}{\varepsilon^2})$ are the uncertainties in the sum and difference of brightness temperatures at the top of atmosphere (TOA) in bands four and five ($T_{45}$, $\Delta T$), the mean emissivity ($\varepsilon$) and the emissivity difference ($\Delta\varepsilon$), respectively. $A_1$, $A_2$, $A_3$, $B_1$, $B_2$, $B_3$ and $D$ are predetermined coefficients. Sections 2.3.1 to 2.3.4 describe the evaluations of these three individual errors ($\delta(LST_1)$, $\delta(LST_2)$, $\delta(WVC)$) and the RSS of uncertainties in LST ($\delta(T_s)$).

#### 2.3.1. Sensitivity to Brightness Temperatures Uncertainty

The noise equivalent differential temperature (NE$\Delta$T) for FY-3B/VIRR bands 4 and 5 are 0.2 K (*i.e.*, $\delta(T_4) = \delta(T_5) = 0.2$) [47]. Hence, the value of 0.28 is used for $\delta(T_{45})$ and $\delta(\Delta T)$ ($\delta(T_{45}) = \delta(\Delta T) = \sqrt{\delta(T_4)^2 + \delta(T_5)^2}$) to investigate the LST error caused by the BT uncertainty ($\delta(LST_1)$).

For example, the sensitivities of BT for the GSW algorithm in dry (WVC in 0–1.5 g/cm$^2$) and wet (WVC in 4–5.5 g/cm$^2$) atmospheric conditions with ε ϵ [0.89, 0.96], LST ϵ [275, 295] K and LST ϵ [305, 325] K are shown in Figure 4a,b, respectively. The same sub-ranges of WVC and LST with ε ϵ [0.94, 1.00] are shown in Figure 4c,d.

We can see from Figure 4 that the values of $\beta_{BT}$ are larger than $\alpha_{BT}$ in all sub-ranges, implying that the GSW algorithms are more sensitive to uncertainty in $\Delta T$ than $T_{45}$. The LST error when ε ϵ [0.89, 0.96] is within [0.63, 0.92] K with a mean of 0.74 K for a dry atmosphere (WVC in 0–1.5 g/cm$^2$) and [0.78, 3.40] K with a mean of 1.49 K for a wet atmosphere (WVC in 4–5.5 g/cm$^2$). The LST error when ε ϵ [0.94, 1.00] is [0.58, 0.90] K with the mean of 0.72 K for a dry atmosphere and [0.69, 3.25] K with a mean of 1.43 K for a wet atmosphere.

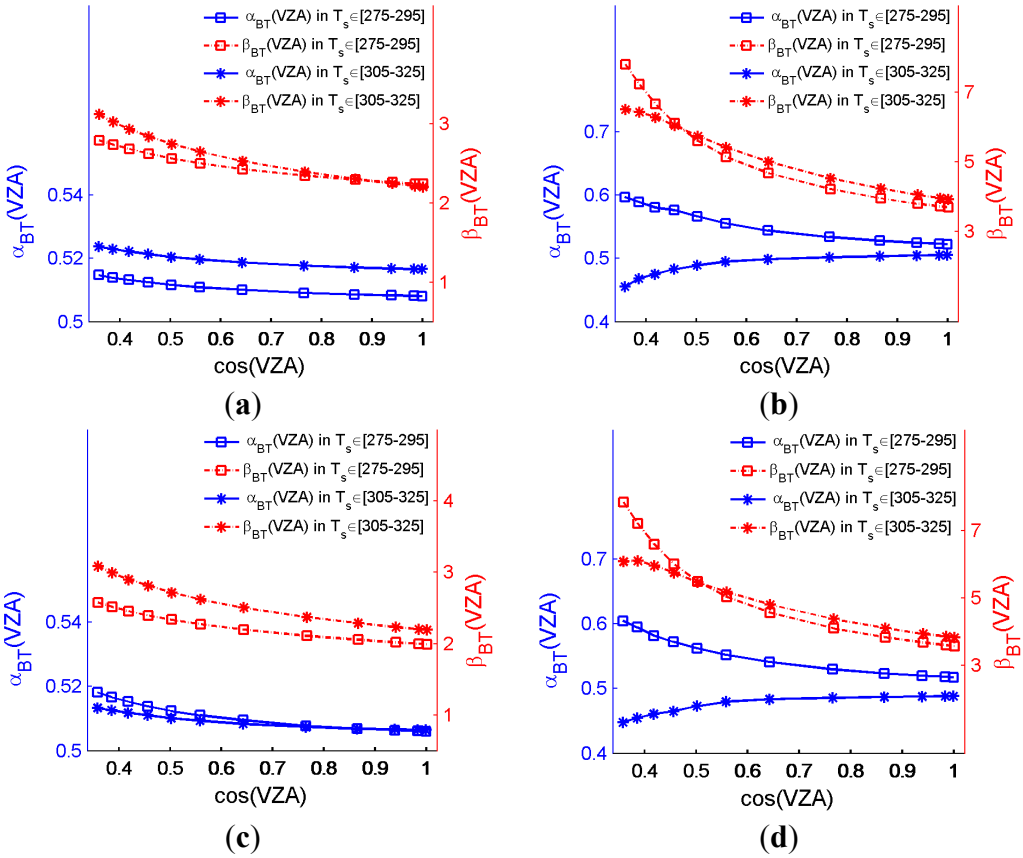


**Figure 4.** Sensitivities of the uncertainty in BT for the FY-3B/VIRR GSW algorithm for the sub-ranges with LST ϵ [275, 295] and LST ϵ [305, 325] K for (**a**) ε ϵ [0.89, 0.96], WVC ϵ [0, 1.5] g/cm$^2$; (**b**) ε ϵ [0.89, 0.96], WVC ϵ [4, 5.5] g/cm$^2$; (**c**) ε ϵ [0.94, 1], WVC ϵ [0, 1.5] g/cm$^2$; (**d**) ε ϵ [0.94, 1], WVC ϵ [4, 5.5] g/cm$^2$.

### 2.3.2. Sensitivity to LSE Uncertainty

The LST error due to the uncertainty in the surface emissivity is $\delta(LST_2)$. For example, the sensitivities of emissivity for the GSW algorithm in dry atmospheric conditions (WVC in 0–1.5 g/cm$^2$) and wet atmospheric conditions (WVC in 4–5.5 g/cm$^2$) with ε ϵ [0.89, 0.96], LST ϵ [275, 295] and LST ϵ [305, 325] K are shown in Figure 5a,b. The same sub-ranges of WVC and LST with ε ϵ [0.94, 1.00] are shown in Figure 5c,d.

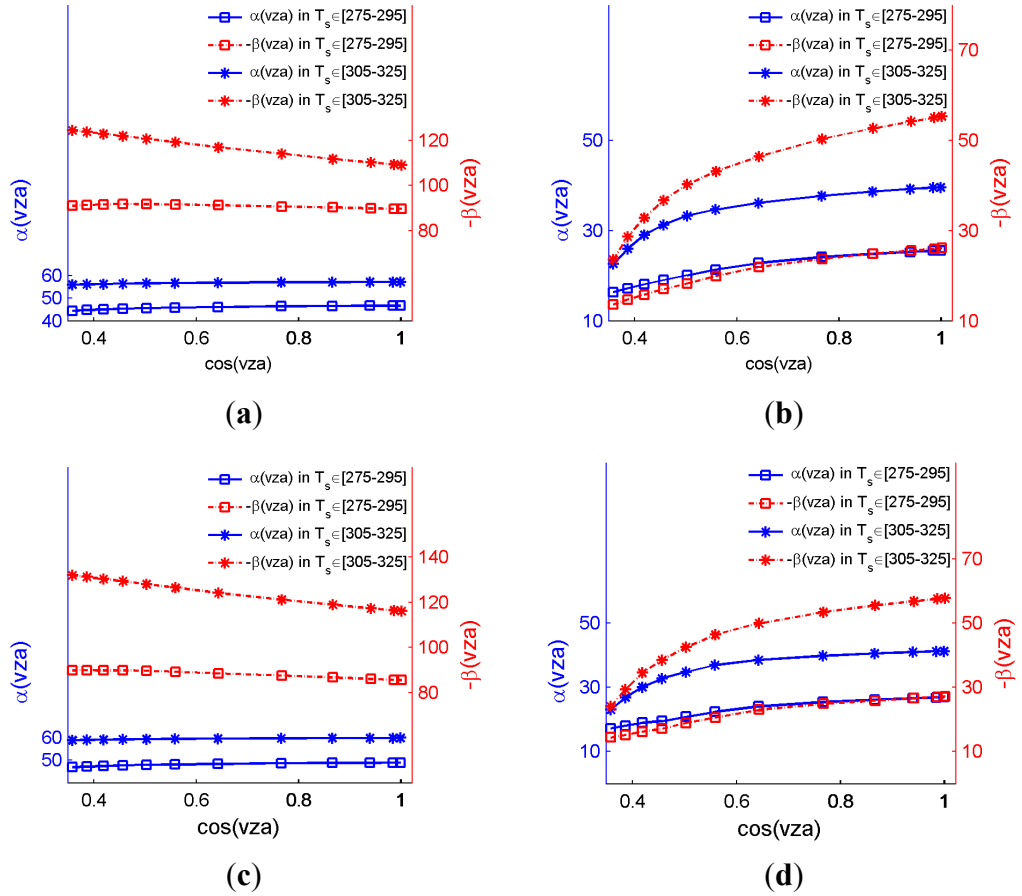


**Figure 5.** Sensitivities of emissivity variations in the GSW algorithm for the sub-ranges with LST ϵ [275, 295] and LST ϵ [305, 325] K for (**a**) ε ϵ [0.89, 0.96], WVC ϵ [0, 1.5] g/cm$^2$; (**b**) ε ϵ [0.89, 0.96], WVC ϵ [4, 5.5] g/cm$^2$; (**c**) ε ϵ [0.94, 1.00], WVC ϵ [0, 1.5] g/cm$^2$; and (**d**) ε ϵ [0.94, 1.00], WVC ϵ [4, 5.5] g/cm$^2$.

We can observe the following from Figure 5:

(a) The values of α and the absolute values of β when LST ϵ [305, 325] K are larger than that those of LST ϵ [275, 295] K for each sub-range, implying that the emissivity sensitivity increases as LST increases, because the emissivity effect is compensated partially by the reflected downward atmospheric radiation.

(b) The absolute values of β are two times greater than α in two LST sub-ranges in dry atmospheric conditions (Figure 5a,c) but are approximately the same in wet atmospheric conditions (Figure 5b,d), indicating that the GSW algorithm is more sensitive to uncertainty in Δε in dry atmospheric conditions. This finding is consistent with the emissivity sensitivity analysis for MODIS, where the sensitivity decreases as WVC increases because of the compensative effect of the reflected downward atmospheric thermal infrared radiation [45].

(c) The value of α (absolute β) at VZA = 0° is approximately two times larger than that at VZA = 69° for a wet atmosphere but is the same for a dry atmosphere, implying that the effect of VZA on both α and β increases from dry to wet atmospheres.

Assuming that the uncertainties of $(1 - \varepsilon)/\varepsilon$ and $\Delta\varepsilon/\varepsilon^2$ are approximately 0.01 for well-known land surfaces [14], the LST error is within [0.88, 1.60] K with a mean of 1.18 K for a dry atmosphere and [0.18, 0.83] K with a mean of 0.40K for a wet atmosphere when ε ϵ [0.89, 0.96]. The LST error is within [0.92, 1.68] K with a mean of 1.23 K for a dry atmosphere and [0.18, 0.89] K with a mean of 0.29 K for a wet atmospheric when ε ϵ [0.94, 1.00].

### 2.3.3. Sensitivity Analysis to Atmospheric WVC

The uncertainty of the atmospheric WVC in the GSW algorithm (*i.e.*, $\delta(WVC)$) is caused by incorrect WVC sub-range selection. An error of ±0.4 g/cm$^{-2}$ is used for low WVC (WVC < 1.5 g/cm$^{-2}$) [48] and an error of 10% is considered for others [49] to numerically analyze the effect of atmospheric WVC uncertainty on the LST retrieval using the GSW algorithm (Equation (1)). $\delta(WVC)$ can be calculated using Equation (4)

$$\delta(WVC) = LST_{\Delta WVC} - LST_{WVC} = LST(WVC + \delta(WVC)) - LST_{WVC} \quad (4)$$

where $LST_{\Delta WVC}$ and $LST_{WVC}$ are the LST retrieved using Equation (1) for the WVC with uncertainty and for the original WVC, respectively.

For example, the *LST* error between $LST_{\Delta WVC}$ and $LST_{WVC}$ for sub-ranges with LST ϵ [290, 310] K and ε in the range (a) 0.89–0.96 and (b) 0.94–1.00 are shown in Figure 6. $\delta(WVC)$ increases as WVC increases at each VZA. The largest RMSEs, which appear in large VZA and a wet atmosphere, are approximately 1.8 and 1.4 K for the sub-ranges with LST ϵ [290, 310] K and ε ϵ [0.89, 0.96] and ε ϵ [0.94, 1.00], respectively.

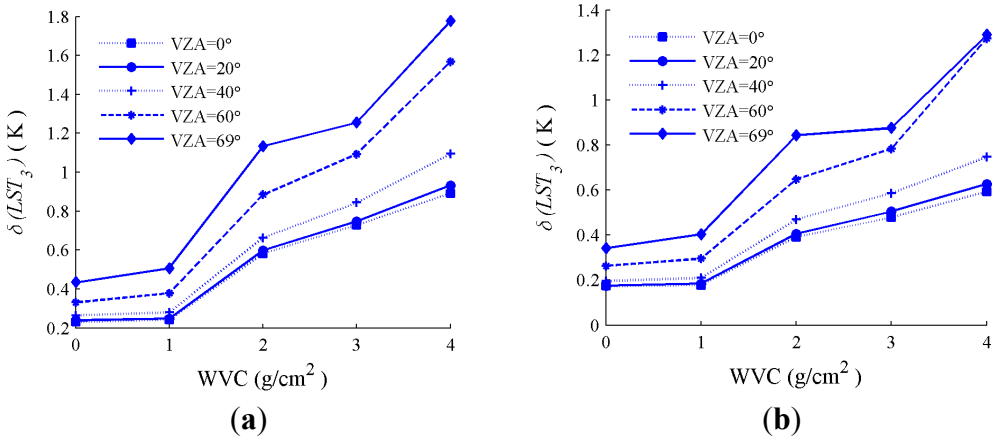


**Figure 6.** The LST error due to uncertainty in the atmospheric WVC for the sub-ranges with LST ϵ [290 K, 310 K] and ε in the range (**a**) 0.89–0.96 and (**b**) 0.94–1.00.

### 2.3.4. Root Sum Square (RSS) of Uncertainties

The RSS of uncertainties in LST retrieved by the GSW algorithm for FY-3B/VIRR with LST ϵ [290, 310] K and ε in the range (a) 0.89–0.96 and (b) 0.94–1.00 are shown in Figure 7. The RSS increases with VZA and rises sharply for wetter atmospheres (WVC > 2 g/cm$^2$) from a VZA of 60°. The maximum RSS nears 1.8 K when VZA ≤ 30° and 3.5 K for VZA = 69°. The individual uncertainties contribution to the RSS of the FY-3B/VIRR GSW algorithm with LST ϵ [290, 310] K

and ε ϵ [0.94, 1.00] for dry and wet atmospheres are listed in Table 1. The primary error source for dry atmospheric conditions is emissivity. The BT provided the largest contribution to the RSS for small VZA (VZA < 40°) for wet atmospheric conditions, and the algorithm error made the largest contribution for larger VZA. Similar results are obtained for other sub-ranges.

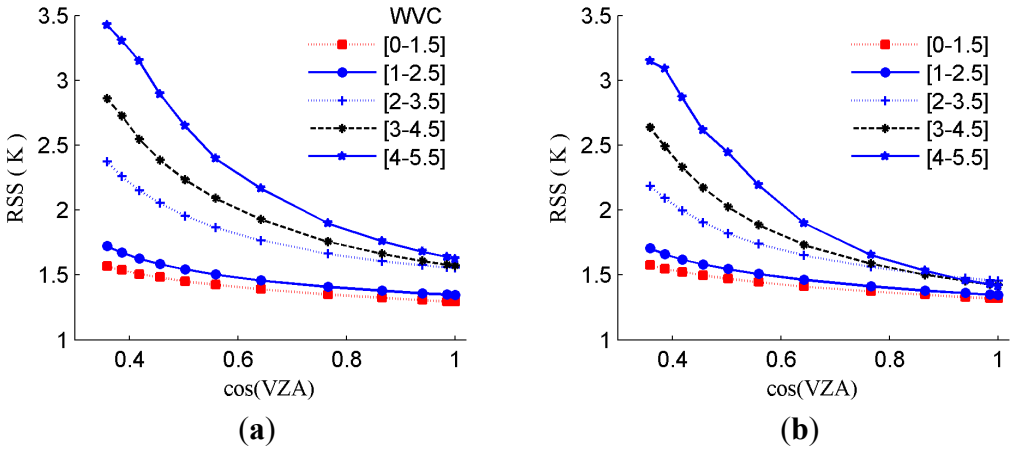


**Figure 7.** Error estimate using RSS of the FY-3B/VIRR GSW algorithm with LST ϵ [290, 310] K, ε ϵ [0.89, 0.96], and ε ϵ [0.94, 1.00] for all WVC sub-ranges. (**a**) ε ϵ [0.89, 0.96], LST ϵ [290, 310]; (**b**) ε ϵ [0.94, 1.00], LST ϵ [290, 310].

**Table 1.** The individual uncertainties contribution to the root sum square (RSS) of the Visible and Infrared Radiometer on FengYun 3B (FY-3B/VIRR) Generalized Split-Window (GSW) algorithm when land surface temperature (LST) ϵ [290, 310] and ε ϵ [0.94, 1.00] for dry and wet atmospheres.

| **Uncertainties** | **Viewing Angle** | | | | |
|---|---|---|---|---|---|
| | **0°** | **20°** | **40°** | **60°** | **69°** |
| | WVC ϵ [0, 1.5], LST ϵ [290, 310], ε ϵ [0.94, 1.00] | | | | |
| error in algorithm | 0.13 | 0.14 | 0.16 | 0.23 | 0.33 |
| 0.01 error in $(1-\varepsilon)/\varepsilon$ and $\Delta\varepsilon/\varepsilon^2$ | 1.15 | 1.16 | 1.18 | 1.22 | 1.24 |
| error due to $\Delta T$ and $T_{45}$ (0.28 K) | 0.61 | 0.62 | 0.66 | 0.75 | 0.85 |
| ±0.4 g/cm$^{-2}$ error in WVC | 0.17 | 0.17 | 0.20 | 0.26 | 0.34 |
| RSS (K) | 1.32 | 1.33 | 1.37 | 1.47 | 1.58 |
| | WVC ϵ [4, 5.5], LST ϵ [290, 310], ε ϵ [0.94, 1.00] | | | | |
| error in algorithm | 0.53 | 0.56 | 0.73 | 1.36 | 2.27 |
| 0.01 error in $(1-\varepsilon)/\varepsilon$ and $\Delta\varepsilon/\varepsilon^2$ | 0.52 | 0.52 | 0.48 | 0.39 | 0.24 |
| error due to $\Delta T$ and $T_{45}$ (0.28 K) | 1.04 | 1.07 | 1.19 | 1.54 | 1.75 |
| 10% error in WVC | 0.59 | 0.63 | 0.75 | 1.27 | 1.29 |
| RSS (K) | 1.41 | 1.46 | 1.66 | 2.44 | 3.15 |

## 3. Evaluation with Ground-Measured LST

### *3.1. Study Area and Datasets*

The ground-measured LST at four barren surface sites (GB, SSW, HZZ, JCHM), which are located in the Heihe River Basin of northwestern China, are used to validate the FY-derived LST (Figure 8). The Heihe River basin is located in an arid climate zone with a low atmospheric WVC [50]. The *in situ* measurements and remotely sensed data used in this study are from the HiWATER field campaign. HiWATER was designed as an ongoing watershed-scale eco-hydrological campaign to address the issues of heterogeneity, scaling, uncertainty and closing of the water cycle on the watershed scale [38]. Three key experimental areas (KEAs) are designed for HiWATER, the cold region experimental area in the upper reaches, the artificial oasis experimental area in the middle reaches, and the natural oasis experimental area downstream. The four sites are located in the KEA of the middle stream.

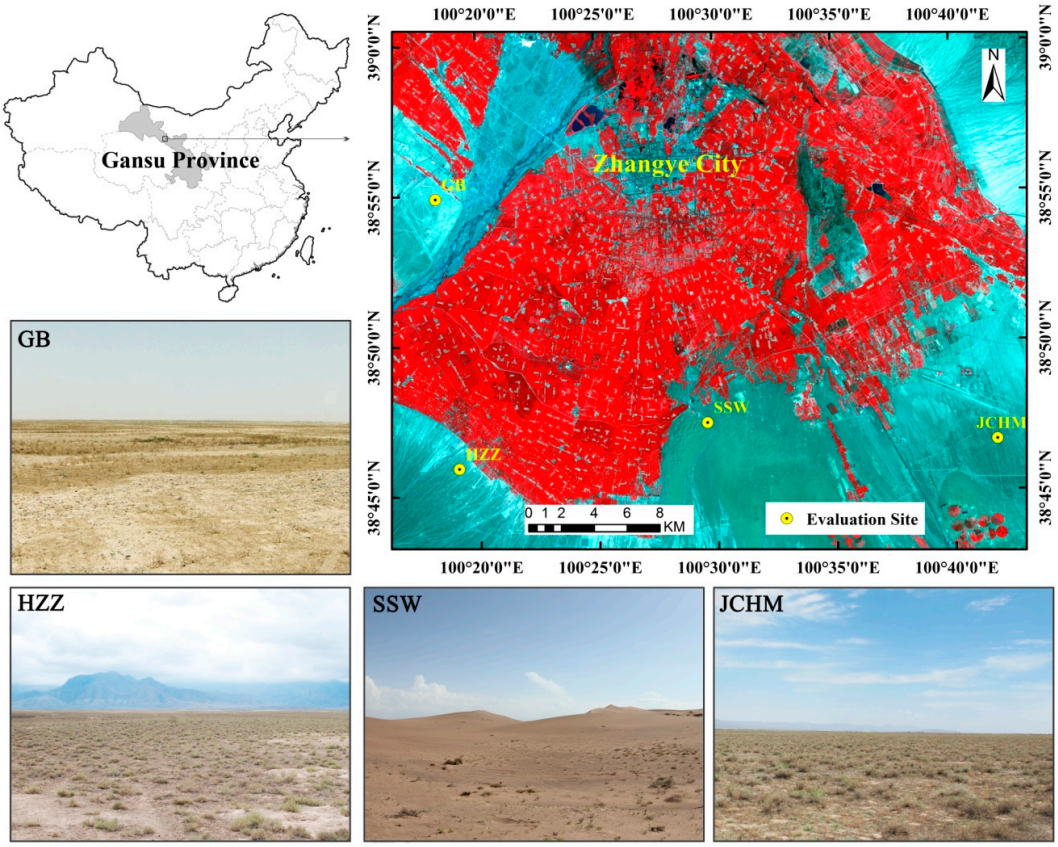


**Figure 8.** The ASTER L1B VNIR image covering the study area on 10 July 2012. The RGB components are channels 3 (0.81 μm), 2 (0.66 μm) and 1 (0.56 μm).

The geographic locations and descriptions of these four sites are presented in Table 2. The land cover types of VIRR/ FY-3B can be obtained from FY-3B/VIRR categories, which are similar to those from the International Geosphere-Biosphere Program (IGBP). The land cover types between FY-3B/VIRR and MODIS_IGBP are different. The four sites according to field surveys consist of three land surface types, Gobi (GB), sand dune (SSW) and desert steppe (HZZ, JCHM). The primary plant type within these sites is *A. sparsifolia* [51], and the desert steppe site has a higher vegetation

coverage than GB and SSW with an *A. sparsifolia* ground cover fraction of approximately 0.1. Therefore, the four sites should be classified as barren soil (Barren or Sparsely Vegetated) rather than the misclassification in the land cover map. However, the three land surface types have different soil types. Gobi consists of small gravel and bare soil, the sand dune is primarily composed of quartz and the desert steppe consists of bare soil. The total WVC for the four sites ranged from 0.04 to 4.72 g/cm$^2$ from June 2012 to December 2013 with a mean of 0.78 g/cm$^2$ according to the atmospheric profile product from MODIS (MOD05).

**Table 2.** Details of the four sites.

| Site | Latitude/Longitude | Elevation (m) | Land Cover | Land Cover type | | Radiometers | Time Period (year/month/day) |
|---|---|---|---|---|---|---|---|
| | | | | VIRR | MODIS_IGBP | | |
| GB | 38.9150°N 100.3042°E | 1567 | Gobi | 7, 16 | 10 | CNR1 | 2012/08/01–2013/12/31 |
| SSW | 38.7892°N 100.4933°E | 1555 | Sand dune | 16 | 10 | CNR1 | 2012/06/08–2013/12/31 |
| HZZ | 38.7652°N 100.3186°E | 1735 | Desert steppe | 7, 16, 10 | 10 | SI-111 | 2012/06/04–2013/12/31 |
| JCHM | 38.7781°N 100.6967°E | 1625 | Desert steppe | 16 | 10 | SI-111 | 2012/06/29–2013/12/31 |

Note: 10 is Grasslands in MODIS IGBP land cover type 7 is Open Shrublands, 10 is Grasslands, and 16 is Barren or Sparsely Vegetated for FY-3B/VIRR.

### *3.2. Ground-Measured LST Estimation*

The GB and SSW sites are equipped with a CNR1 (Kipp & Zonen) net radiometers observe the surface at nadir from 6 m height. The upwelling and downwelling longwave radiation measured by the CNR1 net radiometer is used to estimate LST by:

$$T_s = \left[ \frac{F^{\uparrow} - (1-\varepsilon_b) F^{\downarrow}}{\sigma \varepsilon_b} \right]^{1/4} \tag{5}$$

where $T_s$ is the LST, $F^{\uparrow}$ is the surface upwelling longwave radiation, $\varepsilon_b$ is the surface broadband emissivity (BBE) for 8–13.5 μm, σ is the Stefan–Boltzmann's constant ($5.67 \times 10^{-8}$ Wm$^{-2}$·K$^{-4}$), and $F^{\downarrow}$ is the atmospheric downwelling longwave radiation at the surface. The BBE is estimated from the ASTER narrowband emissivities using a linear equation [52]. The values of BBE are 0.955 ± 0.007 and 0.922 ± 0.005 for GB and SSW sites, respectively [37].

The HZZ site is equipped with two Apogee SI-111 8–14 μm infrared radiometer and directly measure the land surface brightness temperature. SI-111 observe the surface at nadir from 2.65 m height to obtain a target footprint of 3.6 m$^2$. Two SI-111 radiometers are also installed at the JCHM site, one observes an area of 8 m$^2$ at nadir from 4 m height and the other aims the sky at approximately 55° from the zenith measure the atmospheric downwelling longwave radiance. For the HZZ and JCHM sites, the emissivity value of 0.970 ± 0.002 can be used to estimate the true land surface temperature $T_s$ by:

$$B(T_s) = \left( B(T_b) - (1-\varepsilon) L_{\text{atm}}^{\downarrow} \right) \Big/ \varepsilon \tag{6}$$

where $B$ is the Planck function weighted for the spectral response function of the SI-111 radiometer, $\varepsilon$ is the land surface emissivity, and $L_{\text{atm}}^{\downarrow}$ is the downwelling radiance.

These sites are also equipped with other meteorological instruments to measure the magnitudes of the air temperature, humidity and wind speed (except for the JCHM site). For the temperature measurement, the total

uncertainty, included the effects of calibration, emissivity correction, temporal and spatial uncertainty, is 1.65 K, 1.72 K, 0.90 K and 0.75 K for the GB, SSW, HZZ and JCHM sites, respectively [37].

### *3.3. The LST Retrieval*

TOA brightness temperatures, VZA, LSE, and atmospheric WVC from the clear-sky satellite data are required for LST estimation using the GSW algorithm as indicated by Equation (1). The WVC in this study is obtained from the MODIS total precipitable water product (MOD05) with absolute time differences of less than one hour. The satellite observation time is derived by linearly interpolating the start and end times of each FY-3B/VIRR swath. Calculations of the LSE and TOA BT are described in Sections 3.3.1 and 3.3.2.

#### 3.3.1. Calculations of LSE

The classification-based emissivity method (CBEM) [53–55] can be used to estimate LSE for FY-3B/VIRR. This method assigns the emissivity from classification-based look-up tables to each class. However, a previous study indicated that assigning a fixed emissivity value to the barren soil may lead to an overestimation of the spectral emissivity values over very warm arid regions and generally results in an underestimation of the LST over these regions. Using maps of physically retrieved dynamic surface emissivities (like those from ASTER-TES, MODIS MOD11B1 or MOD21 products) as algorithm inputs may improve the inversion accuracy of the GSW algorithm [37,39] for barren surfaces. Hence, the ASTER emissivity dataset is used to calculate the band emissivities of the four evaluation sites. The fixed emissivity value extracted from spectral libraries is also assigned to the four sites to compare accuracy. Two ASTER emissivity datasets are used to calculate the emissivities of two FY-3B/VIRR thermal bands. One database is the ASTER Global Emissivity Database (ASTER_GED) [56]. ASTER_GED products are output as 1° × 1° tiles at 100-m (AG100) or 1-km (AG1 km) spatial resolutions (nominal) and include the mean emissivity and standard deviation for all five ASTER thermal infrared bands, mean land surface temperature (LST) and standard deviation, a re-sampled ASTER GDEM, land-water mask, mean normalized difference vegetation index (NDVI) and standard deviation, latitude, longitude, and observation count, which are developed by the National Aeronautics and Space Administration's (NASA) Jet Propulsion Laboratory (JPL), California Institute of Technology, released by NASA's Land Processes Distributed Active Archive Center (LP DAAC) on 2 April 2014 [57]. The AG1km does not include the years 2012 and 2013; hence, another dataset referred to as ASTER_2012 is used. ASTER_2012 is the average of twelve ASTER emissivity products collected during the HiWATER field campaign from 30 May 2012 to 28 September 2012. ASTER_2012 is derived from ASTER data using the Temperature Emissivity Separation (TES) algorithm [58] combined with the Water Vapor Scaling (WVS) atmospheric correction method [59,60], which is the same algorithm used for generating ASTER_GED products. *In situ* validation indicated that the emissivity accuracy of this algorithm is better than 0.01 for all bands [61]. Previous studies have shown that there are diurnal changes of land surface emissivity due to soil water content variations for the two infrared channels, which might affect the LST retrievals [62]; however, the emissivity values of the four sites can be assumed stable during the evaluation period, because the four sites are barren surfaces, which have a low fraction of vegetation cover with little change, and the surface structures are influenced rarely by human

activity. Thus the average emissivities from ASTER can be used for LST estimation. The fixed emissivity value is calculated using spectral emissivity integrals of soils samples and the spectral response functions of FY-3B/VIRR bands four and five. The spectral emissivities are chosen from two spectral databases, including the John Hopkins University (JHU) spectral library included in the ASTER spectral library [63] and the MODIS-UCSB emissivity library [64]. Finally, 102 soil samples are with a mean emissivity value of 0.9664 ± 0.0106 and 0.9758 ± 0.0061 for bands four and five, respectively, are used. These samples are used to build an LSE statistical relationship between the ASTER and FY-3B/VIRR TIR bands using a multiple linear regression analysis. The emissivity of bare soil in FY-3B/VIRR TIR bands four and five is expressed as a linear combination of emissivities from ASTER bands 13 (10.25–10.95 μm) and 14 (10.95–11.65 μm) using Equation (7). The precision of model fitting is very high through the determination coefficient ($r^2$) and the root-mean square error (RMSE).

$$\begin{aligned} \varepsilon_{TIR4} &= 0.0070 + 0.8882\varepsilon_{ASTER\_13} + 0.1044\varepsilon_{ASTER\_14} \quad R^2 = 0.995 \quad RMSE = 0.001 \\ \varepsilon_{TIR5} &= 0.1968 - 0.1038\varepsilon_{ASTER\_13} + 0.9064\varepsilon_{ASTER\_14} \quad R^2 = 0.939 \quad RMSE = 0.002 \end{aligned} \tag{7}$$

The linear models are applied to calculate the LSE for the four evaluation sites in FY-3B/VIRR bands four and five. Mean emissivities ($\varepsilon_{AG1km}$, $\varepsilon_{2012}$, $\varepsilon_{spec}$) and emissivity differences ($\Delta\varepsilon_{AG1km}$, $\Delta\varepsilon_{2012}$, $\Delta\varepsilon_{spec}$) between FY-3B/VIRR bands four and five, which are derived from AG1km, ASTER_2012 and the emissivity spectral library, are shown in Table 3.

**Table 3**. The values of $\varepsilon_{AG1km}$, $\varepsilon_{2012}$, $\varepsilon_{spec}$, $\Delta\varepsilon_{AG1km}$, $\Delta\varepsilon_{2012}$ and $\Delta\varepsilon_{spec}$ between FY-3B/VIRR bands 4 and 5 at the four sites.

| Site | $\varepsilon_{AG1km}$ | $\Delta\varepsilon_{AG1km}$ | $\varepsilon_{2012}$ | $\Delta\varepsilon_{2012}$ | $\varepsilon_{spec.}$ | $\Delta\varepsilon_{spec.}$ |
|---|---|---|---|---|---|---|
| GB | 0.966 | −0.009 | 0.966 | −0.010 | 0.971 | −0.009 |
| SSW | 0.955 | −0.018 | 0.957 | −0.019 | 0.971 | −0.009 |
| HZZ | 0.971 | −0.005 | 0.975 | −0.006 | 0.971 | −0.009 |
| JCHM | 0.967 | −0.008 | 0.975 | −0.006 | 0.971 | −0.009 |

Table 3 indicates that the value of $\varepsilon_{AG1km}$ is similar to $\varepsilon_{2012}$ at GB and SSW and is smaller than $\varepsilon_{2012}$ at HZZ and JCHM. $\varepsilon_{2012}$ was derived from twelve ASTER emissivity products collected in 2012 summer. The summer of 2012 was a rainy season. Thus, the emissivities of HZZ and JCHM are larger than other seasons because the fraction of vegetation cover and soil water content of these sites are relatively larger. However, the absolute difference between $\varepsilon_{AG1km}$ ($\Delta\varepsilon_{AG1km}$) and $\varepsilon_{2012}$ ($\Delta\varepsilon_{2012}$) is very small for GB, SSW and HZZ sites ($|\varepsilon_{AG1km} - \varepsilon_{2012}| < 0.004$, $|\Delta\varepsilon_{AG1km} - \Delta\varepsilon_{2012}| < 0.001$). The values of $\varepsilon_{spec.}$ ($\Delta\varepsilon_{spec}$) are similar to $\varepsilon_{AG1km}$ ($\Delta\varepsilon_{AG1km}$) for GB, HZZ and JCHM but are perceptibly larger for SSW. Hence, assigning the same emissivity value for the barren surface is unreasonable, especially for the sand dunes, which have low emissivity values.

### 3.3.2. Determination of the TOA BT

The TOA brightness temperatures $T_4$ and $T_5$ are calculated according to the infrared channel calibration method of FY-3B/VIRR. The accuracies of radiometric calibration for FY-3B/VIRR TIR bands from January 2012 to June 2013 are evaluated using the Low Earth Orbit (LEO)-LEO simultaneous nadir overpass intercalibration method [65]. Results indicate that the BT measured from

FY-3B/VIRR is consistent with that from Infrared Atmospheric Sounder Interferometer (IASI), and the annual mean biases are 0.84 ± 0.16 and −0.66 ± 0.18 K for bands four and five, respectively, which are unconcerned with scene temperature dependence and seasonal variation. The recalibration values of $T_4$ and $T_5$ from July 2012 to June 2013 are obtained from Xu *et al.* [65], and annual mean biases of 0.84 and −0.66 K for bands four and five are assigned to other times.

The clear-sky FY-3B/VIRR data for the four sites are used to retrieve LST using the GSW algorithm. Because an accurate cloud filter for the satellite data is critical for reliable results and a FY-3B/VIRR cloud mask product is unavailable, the standard MODIS cloud mask product (MYD35) is used. We only use data with an absolute overpass time difference between AQUA/MODIS and FY-3B/VIRR of less than one hour. Finally, the cloud-free FY-3B/VIRR LST is matched with the ground-measured LST according to the satellite observation time. It should be noted that masking errors exist in all cloud-mask products and cloud mask may change due to the overpass time difference. All valid points in the daytime are examined manually to exclude undetected clouds or poor data pixel quality to minimize the effect of cloud contamination in validation results in this work.

### *3.4. Results and Discussion*

FY-3B/VIRR LST obtained using the emissivity derived from AG1km, ASTER_2012 and spectral library are referred to as $T_{AG1km}$, $T_{2012}$ and $T_{Spec}$, respectively. The LST of the four sites calculated using the above GSW algorithm with three different emissivity values are all compared with the ground-measured LST (*i.e.*, $T_g$). The biases (FY-3B/VIRR LST−ground-measured LST), standard deviation (STD) and root mean squared errors (RMSEs) for each site are summarized in Tables 4 and 5 for the nighttime and the daytime, respectively.

The biases and RMSEs of $T_{AG1km}$ and $T_{2012}$ for the nighttime results are similar for the four sites, with average biases of −0.04 and −0.17 K and average RMSEs of 1.38 K and 1.43 K for $T_{AG1km}$ and $T_{2012}$, respectively. $T_{spec}$ has a larger bias and RMSE than $T_{AG1km}$ and $T_{2012}$ with an average bias of −0.41 K and average RMSE of 1.70 K for the four sites, which means using an ASTER-derived emissivity product for LST retrieval can achieve higher accuracy for barren surface. This result is more obvious for the SSW site, where $T_{spec}$ significantly underestimates the LST by more than 1.7 K compared with $T_{AG1km}$ due to overestimated emissivity.

**Table 4.** Summary of nighttime evaluation results for FY-3B/VIRR at the four sites.

| Site | Bias | | | STD | | | RMSE | | | N |
|---|---|---|---|---|---|---|---|---|---|---|
| | $T_{AG1km} - T_g$ | $T_{2012} - T_g$ | $T_{Spec} - T_g$ | $T_{AG1km} - T_g$ | $T_{2012} - T_g$ | $T_{Spec} - T_g$ | $T_{AG1km} - T_g$ | $T_{2012} - T_g$ | $T_{Spec} - T_g$ | |
| GB | −0.28 | −0.17 | −0.47 | 1.38 | 1.38 | 1.38 | 1.41 | 1.38 | 1.45 | 279 |
| SSW | −0.08 | −0.08 | −1.77 | 1.20 | 1.20 | 1.21 | 1.20 | 1.20 | 2.14 | 271 |
| HZZ | 0.61 | 0.54 | 1.08 | 1.63 | 1.62 | 1.62 | 1.73 | 1.71 | 1.94 | 235 |
| JCHM | −0.30 | −0.84 | −0.31 | 1.13 | 1.13 | 1.13 | 1.17 | 1.41 | 1.17 | 290 |
| ALL | −0.04 | −0.17 | −0.41 | 1.38 | 1.42 | 1.65 | 1.38 | 1.43 | 1.70 | 1075 |

**Table 5.** Summary of daytime evaluation results for FY-3B/VIRR at the four sites.

| Site | Bias | | | STD | | | RMSE | | | N |
|---|---|---|---|---|---|---|---|---|---|---|
| | $T_{AG1km} - T_g$ | $T_{2012} - T_g$ | $T_{Spec} - T_g$ | $T_{AG1km} - T_g$ | $T_{2012} - T_g$ | $T_{Spec} - T_g$ | $T_{AG1km} - T_g$ | $T_{2012} - T_g$ | $T_{Spec} - T_g$ | |
| GB | −1.60 | −1.50 | −1.85 | 2.06 | 2.06 | 2.06 | 2.60 | 2.54 | 2.76 | 207 |
| SSW | −0.10 | −0.12 | −2.05 | 2.22 | 2.22 | 2.10 | 2.21 | 2.21 | 2.93 | 229 |
| HZZ | −1.17 | −1.28 | −0.70 | 2.71 | 2.71 | 2.70 | 2.95 | 2.99 | 2.78 | 202 |
| JCHM | −2.23 | −2.89 | −2.28 | 1.95 | 1.99 | 1.95 | 2.96 | 3.51 | 3.00 | 221 |
| ALL | −1.26 | −1.44 | −1.74 | 2.38 | 2.47 | 2.29 | 2.69 | 2.85 | 2.87 | 859 |

The accuracy of $T_{AG1km}$ and $T_{2012}$ are also better than $T_{spec}$ for the daytime results, except for the JCHM site, which is similar to the nighttime results. Because the $\varepsilon_{2012}$ are overestimated by approximately 0.008 compared with the $\varepsilon_{AG1km}$ for JCHM site, which would result in an underestimation of LST. The average bias is −1.26 K, −1.44 K and −1.74 K and the average RMSE is 2.69, 2.85 and 2.87 K for $T_{AG1km}$, $T_{2012}$ and $T_{spec}$, respectively. The daytime biases are negative for the four sites, indicating an underestimation of the LST for barren surface types. The JCHM site has the largest bias (−2.23, −2.89, −2.28K) for all three emissivity values. The largest bias difference between $T_{AG1km}$ and $T_{spec}$ is near 2 K at SSW, which is larger than the nighttime result because there exists a greater heterogeneity of LST during daytime. The accuracy improves significantly at the sand dune site (SSW) when the emissivity derived from AG1km is used, which is consistent with previous studies indicating that the ASTER-derived emissivities for sand dunes is in good agreement with ground measurements [66].

The RMSE values in Tables 4 and 5 show that the difference between $T_{AG1km}$ and $T_g$ is slightly smaller than the difference between $T_{2012}$ and $T_g$, meaning $T_{AG1km}$ has a slightly higher accuracy than $T_{2012}$. Therefore, the following analysis is based on $T_{AG1km}$. Figure 9 shows the scatterplots between ground-measured LST ($T_g$) and $T_{AG1km}$ at the four sites. It shows that the LST algorithm works well at SSW site for both nighttime and daytime and works well at GB, HZZ and JCHM for nighttime. However, its performance for daytime at these three site is slightly bad, especially at JCHM. Previous MODIS C5 LST validation indicated two possible sources for the large LST errors for the split-window algorithm for the barren surface type [21]. First, the original split-window algorithm does not completely cover the wide range of LST; namely, the daytime LST are larger than the $T_{air}$ at the surface by more than 16 K, which is beyond the upper limit ($T_{air}$ + 16 K) used in the current MODIS C5 LST product algorithm development. Second, the large errors in the surface emissivity values in MODIS bands 31 and 32 are estimated from land cover types. However, these issues have been considered in the development of the algorithm in this work. An air temperature upper limit of $T_{air}$ + 29 K can cover the range of LST at the four sites based on Table 6, which shows the differences between the ground-measured LST and the 5-m $T_{air}$ for the daytime. As indicated by the sensitivity analysis in Section 2.3.2, the LST algorithm is more sensitive to uncertainty in emissivity in higher LST conditions. The four sites are in the hot zone with higher LST in the daytime, where a slight emissivity error, especially for the error in $\Delta\varepsilon$, will lead a larger error in the LST. Daytime LST have a larger bias because ASTER TIR bands 13 and 14 do not match the FY-3B/VIRR band five well and the ASTER emissivity products have errors [67]. Additionally, the errors in the satellite data, such as the accuracy of geometrical correction and radiometrical calibration, also influence the retrieval accuracy. Moreover, the

fact that the uncertainty in ground-measured LST, like ground instrument calibration, tower installations, and LST spatial variations, cannot be represented by only one point may also contribute to the errors.

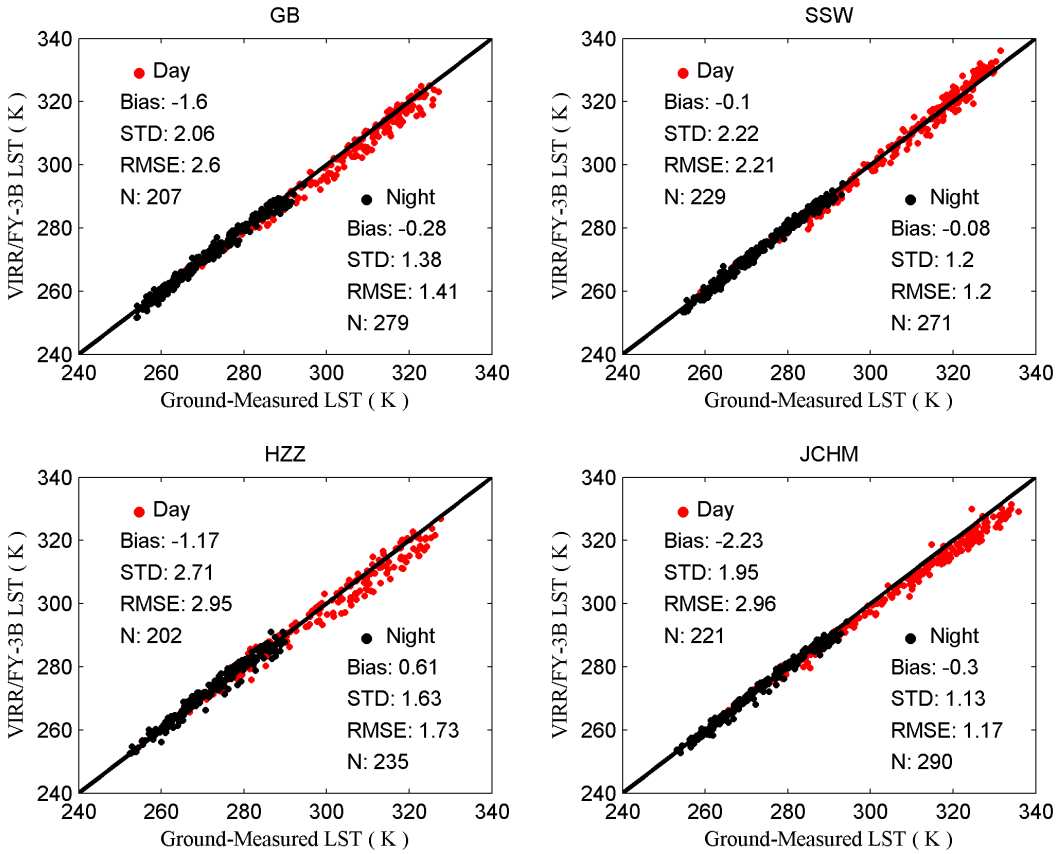


**Figure 9.** Scatterplots between the FY-3B/VIRR LST and ground LST for daytime and the nighttime at the four sites.

**Table 6.** Difference statistics between the ground-measured LST and $T_{air}$ for the daytime in summer.

| Site | Bias | Std |
|---|---|---|
| GB | 16.81 | 3.30 |
| SSW | 21.62 | 2.91 |
| HZZ | 19.86 | 5.83 |

A series of correlation tests are completed between the LST difference (*i.e.*, $\Delta LST$ = FY-3B/VIRR LST − ground-measured LST) and other related variables to further analyze the potential factors that may cause the errors, which include the FY-3B/VIRR sensor view zenith angle (θ), soil water content at 2 cm underground, surface air humidity at 5 m, wind speed at 5 m, $T_{air}$ at 5 m, $T_g$, and the difference between $T_g$ and $T_{air}$. The statistical results and sccatterplots between $\Delta LST$ and these variables are shown in Table 7 and Figure 10, respectively. Because these ground-measurements for the JCHM site are unavailable, only three sites are used for analysis. Table 7 and Figure 10 show that there are no obvious correlations between $\Delta T$ and these variables, and the overall coefficients of determination $r^2$ are small (<0.1) for both daytime and nighttime. Hence, the LST results of this work are independent of these variables. It should be noted that only one year and a half of the LST data are used for analysis; the

amount of the data may not suffice to obtain a clear conclusion. Moreover, the impacts from these variables are intricate and interact among one another [68]. More long-term data are needed to perform a comprehensive evaluation in the future, such as long-term measurements from the Surface Radiation budget (SURFRAD) network.

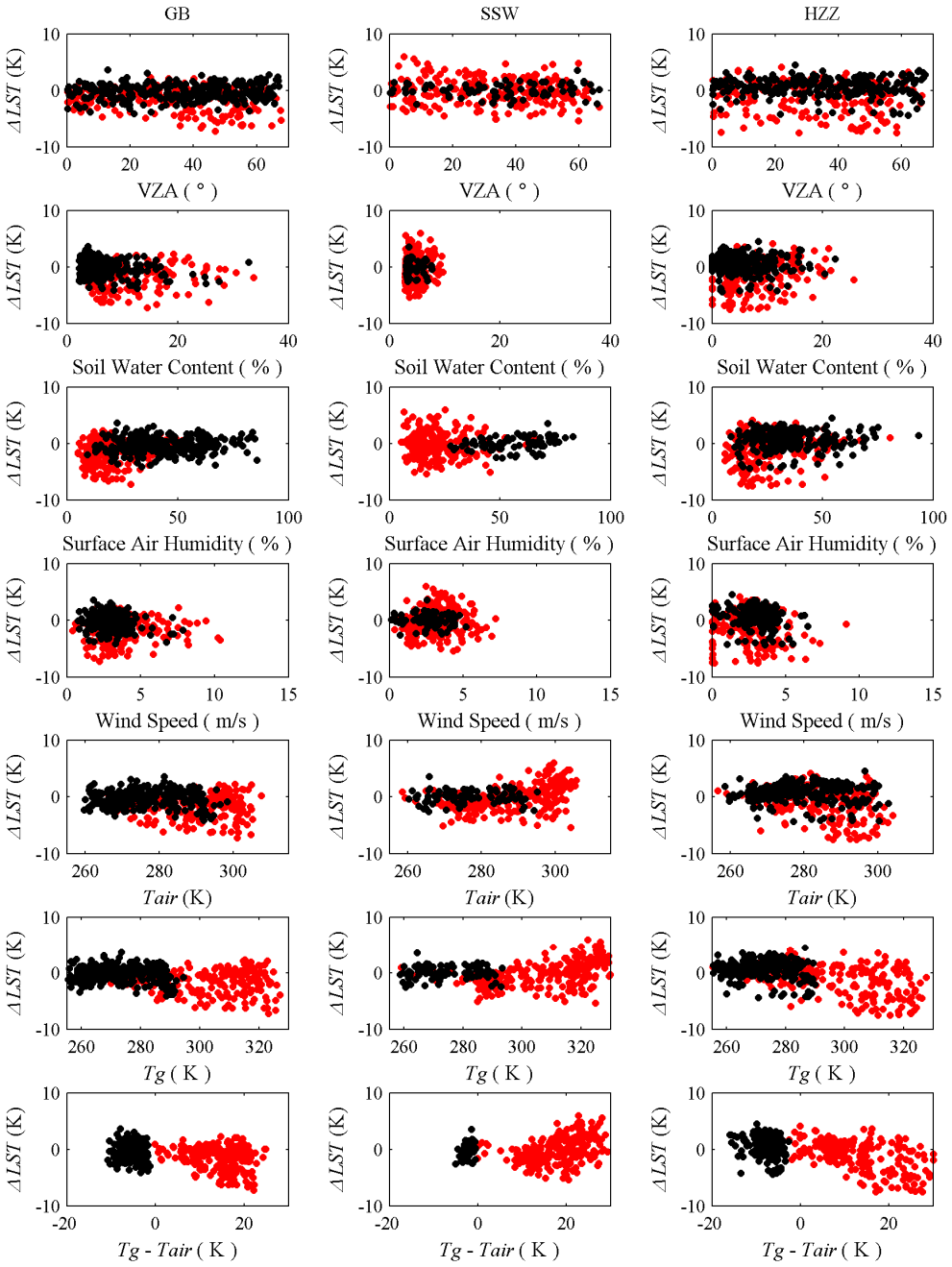


**Figure 10.** Relationship between *ΔLST* and sensor VZA, soil water content, surface air humidity, wind speed, $T_{air}$, $T_g$, and the difference between $T_g$ and $T_{air}$ for daytime (**red dot**) and nighttime (**black dot**).

**Table 7.** The $r^2$ between *ΔLST* and sensor view zenith angles (VZA), soil water content, surface air humidity, wind speed, $T_{air}$ (5 m), $T_g$ and the difference between $T_g$ and $T_{air}$ for daytime and nighttime.

| Variable | All | | GB | | SSW | | HZZ | |
|---|---|---|---|---|---|---|---|---|
| | $R^2$ | | $R^2$ | | $R^2$ | | $R^2$ | |
| | Daytime | Nighttime | Daytime | Nighttime | Daytime | Nighttime | Daytime | Nighttime |
| VZA | 0.010 | 0.002 | 0.050 | 0.009 | 0.009 | 0.006 | 0.015 | 0 |
| Soil Water Content | 0 | 0.013 | 0 | 0.021 | 0 | 0.001 | 0.055 | 0.003 |
| Surface Air Humidity | 0.013 | 0 | 0.015 | 0.002 | 0.002 | 0.099 | 0.030 | 0.004 |
| Wind Speed | 0.013 | 0 | 0.007 | 0.036 | 0.015 | 0.013 | 0.029 | 0.004 |
| $T_{air}$ | 0.012 | 0 | 0.003 | 0.004 | 0.208 | 0.001 | 0.028 | 0.004 |
| $T_g$ | 0.073 | 0.002 | 0.016 | 0.002 | 0.193 | 0.004 | 0.201 | 0.002 |
| $T_g - T_{air}$ | 0.014 | 0.002 | 0.063 | 0.009 | 0.121 | 0.006 | 0.030 | 0 |

## 4. Conclusions

A refined GSW algorithm proposed by Wan [21] is presented in this paper to retrieve LST from FY-3B/VIRR data. MODTRAN 4.0 and TIGR-3 are used to create a simulation database to fit the algorithm coefficients. The average emissivity, WVC, LST are divided into several sub-ranges in each VZA to improve retrieval accuracy. The simulation analysis show that the fitting RMSEs are less than 1.0 K for all sub-ranges when VZA ≤ 30° and WVC < 4.5 g/cm$^2$.

A sensitivity analysis is completed to determine the uncertainty in the brightness temperatures (due to NEΔT), the LSE and the WVC. The results showed that, given an instrument noise NEΔT = 0.2 K, 1% uncertainties in (1 − ε)/ε and Δε/ε$^2$, and an error of ±0.4 g/cm$^{-2}$ in low WVC (*WVC < 1.5 g*/cm$^{-2}$) [48] and an error of 10% for others, the maximum RSS in sub-ranges of LST ϵ [290, 310] K and ε in ranges of 0.89–0.96 and 0.94–1.00 nears 1.8 K when VZA ≤ 30° but is close to 3.5 K for VZA = 69°.

Finally, the long-term ground-measured LST for the four sites during the period of June 2012 to December 2013 collected during the HiWATER field campaign is used to evaluate the GSW algorithm of FY-3B/VIRR. Three emissivity databases are used to estimate the LST, including the ASTER Global Emissivity Database (ASTER_GED) at a 1-km spatial resolution (AG1km), an average of twelve ASTER emissivity data in the 2012 summer and emissivity spectra extracted from spectral libraries. The best results are obtained from the emissivity derived from AG1 km for the four sites with an average bias of 1.26 and −0.04 K and an average RMSE of 2.69 and 1.38 K during daytime and nighttime, respectively. The sand dune site (SSW) is the most improved site, with an improved bias from −1.77 to −0.1 K and from −2.05 to −0.1 K for nighttime and daytime, respectively. Hence, ASTER_GED is a useful emissivity dataset for generating global LST products from different thermal infrared databases, especially for barren surfaces. In the future, the FY-3B/VIRR LST products will be evaluated over different locations and different periods with *in situ* LST measurements, such as using measurements from the SURFRAD network. Besides, the MODIS C6 LST products with high accuracy will also be used to cross-validate the FY-3B/VIRR LST product.

**Acknowledgments**

This work was supported in part by National High-Technology Research and Development Program of China (863 Project: 2012AA12A304), Chinese Natural Science Foundation Project (91125003, 41101325, 41171282), National Basic Research Program of China(2013CB733401) and Chinese Academy of Sciences Action Plan for West Development Project (KZCX2-XB3-15). The authors are grateful to Dr. Na Xu for providing the recalibration values to the study.

**Author Contributions**

Jinxiong Jiang was the principal author for this paper. Jinxiong Jiang, Qinhuo Liu and Hua Li worked on the methodology, sensitivity analysis, the processing of the ground-measured data, the LST retrieval and evaluation. Bo Zhong and Shanlong Wu collected and processed the FY-3B/VIRR data. Heshun Wang, Biao Cao and Yongming Du gave the suggested correction of the final version.

**Conflicts of Interest**

The authors declare no conflict of interest.

**References**

1. Camillo, P.J. Using one- or two-layer models for evaporation estimation with remotely sensed data. In *Land Surface Evaporation, Measurements and Parameterization*; Schmugge, T.J., André, J.C., Eds.; Springer New York: New York, NY, USA, 1991; pp. 183–197.
2. Schmugge, T.J.; Becker, F.; Li, Z.L. Spectral emissivity variations in airborne surface temperature measurements. *Remote Sens. Environ.* **1991**, 35, 95–104.
3. Zhang, L.; Lemeur, R.; Goutorbec, J.P. A one-layer resistance model for estimating regional evapotranpiration using remote sensing data. *Agric. For. Meteorol.* **1995**, *77*, 241–261.
4. Anderson, M.C.; Norman, J.M.; Diak, G.R.; Mecikalski, J.R. A two-source time-integrated model for estimating surface fluxes using thermal infrared remote sensing. *Remote Sens. Environ.* **1997**, *60*, 195–216.
5. Su, Z. The surface energy balance system (SEBS) for estimation of turbulent heat fluxes. *Hydrol. Earth Syst. Sci.* **2002**, *6*, 85–100.
6. Weng, Q.H.; Lu, D.S.; Schubring, J. Estimation of land surface temperature-vegetation abundance relationship for urban heat island studies. *Remote Sens. Environ.* **2004**, *89*, 467–483.
7. Zhou, L.; Dickinson, R.E.; Tian, Y.; Jin, M.; Ogawa, K.; Yu, H.; Schmugge T. A sensitivity study of climate and energy balance simulations with use of satellite-derived emissivity data over Northern Africa and the Arabian Peninsula. *J. Geophys. Res.* **2003**, *108*, doi:10.1029/2003JD004083.
8. Kustas, W.; Anderson, M. Advances in thermal infrared remote sensing for land surface modeling. *Agric. For. Meteorol.* **2009**, *149*, 2071–2081.
9. Anderson, M.C., Hain, C.R.; Wardlow, B.; Mecikalski, J.R.; Kustas, W.P. Evaluation of a drought index based on thermal remote sensing of evapotranspiration over the continental U.S. *J. Clim.* **2011**, *24*, 2025–2044.

10. Anderson, M.C.; Allen, R.G.; Morse, A.; Kustas, W.P. Use of Landsat thermal imagery in monitoring evapotranspiration and managing water resources. *Remote Sens. Environ.* **2012**, *122*, 50–65.
11. Li, Z.L.; Tang, B.H.; Wu, H.; Ren, H.Z.; Yan, G.J.; Wan, Z.M; Trigo, I.F.; Sobrino, J.A. Satellite-derived land surface temperature: Current status and perspectives. *Remote Sens. Environ.* **2013**, *131*, 14–37.
12. Liu, Y.; Hiyama, T.; Yamaguchi, Y. Scaling of land surface temperature using satellite data: A case examination on ASTER and MODIS products over a heterogeneous terrain area. *Remote Sens. Environ.* **2006**, *105*, 115–128.
13. Neteler, M. Estimating daily land surface temperatures in mountainous environments by reconstructed MODIS LST data. *Remote Sens.* **2010**, *2*, 333–351.
14. Wan, Z.; Dozier, J.A. Generalized split-window algorithm for retrieving land-surface temperature from space. *IEEE Trans. Geosci. Remote Sens.* **1996**, *34*, 892–905.
15. Dash, P.; Gfttsche, F.M.; Olesen, F.S.; Fischer, H. Land surface temperature and emissivity estimation from passive sensor data: Theory and practice-current trends. *Int. J. Remote Sens.* **2002**, *23*, 2563–2594.
16. Prata, A.J.; Caselles, V.; Coll, C.; Sobrino, J.A.; Ottlé, C. Thermal remote sensing of land surface temperature from satellites: Current status and future prospects. *Remote Sens. Rev.* **1995**, *12*, 175–224.
17. Anding, D.; Kauth, R. Estimation of sea surface temperatures from space. *Remote Sens. Environ.* **1970**, *1*, 217–220.
18. Price, J.C. Land surface temperature measurements from the split window channels of the NOAA 7 AVHRR. *J. Geophys. Res.* **1984**, *89*, 7231–7237.
19. Kerr, Y.H.; Lagouarde, J.P.; Imbernon, J. Accurate land surface temperature retrieval from AVHRR data with use of an improved split window algorithm. *Remote Sens. Environ.* **1992**, *41*, 197–209.
20. Pinheiro, A.C.T.; Privette, J.L.; Mahoney, R.; Tucker, C.J. Directional effects in a daily AVHRR land surface temperature dataset over Africa. *IEEE Trans. Geosci. Remote Sens.* **2004**, *42*, 1941–1954.
21. Wan, Z. New refinements and validation of the MODIS land-surface temperature/emissivity products. *Remote Sens. Environ.* **2008**, *112*, 59–74.
22. Wan, Z. New refinements and validation of the collection-6 MODIS land-surface temperature/emissivity product. *Remote Sens. Environ.* **2014**, *140*, 36–45.
23. Rozenstein, O.; Qin, Z.; Derimian, Y.; Karnieli, A. Derivation of land surface temperature for Landsat-8 TIRS using a split window algorithm. *Sensors* **2014**, *14*, 5768–5780.
24. Du, C.; Ren, H.Z.; Qin, Q.M.; Meng, J.J.; Zhao, S.H. A practical split-window algorithm for estimating land surface temperature from landsat 8 Data. *Remote Sens.* **2015**, *7*, 647–665.
25. Jiang, J.; Liu, Q.; Li H.; Huang H. Split-window method for land surface temperature estimation from FY-3A/VIRR data. In Proceedings of the International Symposium on Remote Sensing Environ (IGARSS), Vancouver, BC, Canada, 24–29 July 2011; pp. 305–308.
26. Jiang, G.M. Development of split-window algorithm for land surface temperature estimation from the VIRR/FY-3A measurements. *IEEE Geosci. Remote Sens. Lett.* **2013**, *10*, 952−956.

27. Tang, B.H.; Shao, K.; Li, Z.L.; Wu, H.; Nerry, F.; Zhou, G. Estimation and validation of land surface temperatures from Chinese second-generation polar-orbit FY-3A VIRR data. *Remote Sens.* **2015**, *7*, 3250–3273.
28. Trigo, I.F.; Peres, L.F.; DaCamara, C.C.; Freitas, S.C. Thermal land surface emissivity retrieved from SEVIRI/Meteosat. *IEEE Trans. Geosci. Remote Sens.* **2008**, *46*, 307–315.
29. Jiang, G.M.; Li, Z.L. Split-window algorithm for land surface temperature estimation from MSG1-SEVIRI data. *Int. J. Remote Sens.* **2008**, *29*, 6067–6074.
30. Gao, C.X.; Tang, B.H.; Wu, H.; Jiang, X.G.; Li, Z.L. A generalized split-window algorithm for land surface temperature estimation from MSG-2/SEVIRI data. *Int. J. Remote Sens.* **2013**, *34*, 4182–4199.
31. Coll, C.; Valor, E.; Galve, J.M.; Mira, M.; Bisquert, M.; García-Santos, V.; Caselles, E.; Caselles, V. Long-term accuracy assessment of land surface temperatures derived from the Advanced Along-Track Scanning Radiometer. *Remote Sens. Environ.* **2012**, *116*, 211–225.
32. Sun, D.; Yu, Y.; Fang, L.; Liu, Y. Toward an operational land surface temperature algorithm for GOES. *J. Appl. Meteor. Climatol.* **2013**, *52*, 1974–1986.
33. Tang, B.H.; Bi, Y.Y.; Li, Z.L.; Xia, J. Generalized split-window algorithm for estimate of land surface temperature from Chinese geostationary FengYun meteorological satellite (FY-2C) data. *Sensors* **2008**, *8*, 933–951.
34. Wan, Z.; Zhang, Y.; Zhang, Q.; Li, Z.L. Validation of the land-surface temperature products retrieved from Terra Moderate Resolution Imaging Spectroradiometer data. *Remote Sens. Environ.* **2002**, *83*, 163–180.
35. Wan, Z.; Zhang, Y.; Zhang, Q.; Li, Z.L. Quality assessment and validation of the MODIS global land surface temperature. *Int. J. Remote Sens.* **2004**, *25*, 261–274.
36. Wan, Z.; Li, Z.L. Radiance-based validation of the V5 MODIS land-surface temperature product. *Int. J. Remote Sens.* **2008**, *29*, 5373–5395.
37. Li, H.; Sun, D.; Yu, Y.; Wang, H.; Liu, Y.; Liu, Q.; Du, Y.; Wang, H.; Cao, B. Evaluation of the VIIRS and MODIS LST products in an arid area of Northwest China. *Remote Sens. Environ.* **2014**, *142*, 111–121.
38. Li, X.; Cheng, G.; Liu, S.; Xiao, Q.; Ma, M.; Jin, R.; Che, T.; Liu, Q.; Wang, W.; Qi, Y.; *et al.* Heihe watershed allied telemetry experimental research (HiWATER): Scientific objectives and experimental design. *Bull. Am. Meteorol. Soc.* **2013**, *94*, 1145–1160.
39. Guillevic, P.C.; Biard, J.C.; Hulley, G.C.; Privette, J.L.; Hook, S.J.; Olioso, A.; Göttsche, F.M.; Radocinski, R.; Román, M.O.; Yu, Y.; Csiszar, I. Validation of Land Surface Temperature products derived from the Visible Infrared Imaging Radiometer Suite (VIIRS) using ground-based and heritage satellite measurements. *Remote Sens. Environ*. **2014**, *154*, 19–37.
40. Coll, C.; Caselles, C.; Sobrino. J.A.; Valor, E. On the atmospheric dependence of the split-window equation for land surface temperature. *Int. J. Remote Sens.* **1994**, *15*, 1915–1932.
41. Li, Z.L.; Petitcolin, F.; Zhang, R.H. A physically based algorithm for land surface emissivity retrieval from combined mid-infrared and thermal infrared data. *Sci. China* (*Ser. E*) **2000**, *43*, 23–33.
42. Berk, A.; Bernstein, L.S.; Anderson, G.P.; Acharya, P.K.; Robertson, D.C. MODTRAN cloud and multiple scattering upgrades wit application to AVIRIS. *Remote Sens. Environ.* **1998**, *65*, 367–375.

43. Atmospheric Radiation Analysis Laboratoire de Météorologie Dynamique/CNRS/IPSL. Available online: http://ara.abct.lmd.polytechnique.fr/index.php?page=tigr (accessed on 1 December 2010).
44. Kondratyev, K.Y. *Radiation in the Atmosphere*, 1st ed.; Academic Press: New York, NY, USA, 1969; p. 911.
45. Wan, Z. MODIS Land-Surface Temperature Algorithm Theoretical Basis Document (LST ATBD), Version 3.3. Santa Barbara: University of California. Available online: http://modis.gsfc.nasa.gov/data/atbd/atbd_mod11.pdf (accessed on 1 July 2014).
46. Hulley, G.C.; Hook S.J.; Schneider P. Optimized split-window coefficients for deriving surface temperatures from inland water bodies. *Remote Sens. Environ.* **2011**, *115*, 3758–3769.
47. FENGYUN Satellite Data Center. Visible-Infrared Light Scanning Radiometer (VIRR). Available online: http://fy3.satellite.cma.gov.cn/PortalSite/StaticContent/DeviceIntro_FY3_VIRR.aspx? (accessed on 22 July 2014).
48. Galve, J.M.; Coll, C.; Caselles, V.; Valor, E. An atmospheric radiosounding database for generating land surface temperature algorithms. *IEEE Trans. Geosci. Remote Sens.* **2008**, *46*, 1547−1557.
49. Seemann, S.W.; Borbas, E.E.; Li, J.; Menzel, W.P.; Gumley, L.E. *MODIS Atmospheric Profile Retrieval Algorithm Theoretical Basis Document*; University Wisconsin-Madison: Madison, WI, USA, 2006.
50. Wang, K.L.; Cheng, G.D.; Jiang, H.; Zhang, L.J. Atmospheric hydrologic cycle over the Qilian−Heihe valley. *Adv. Water Sci.* **2003**, *14*, 91−97.
51. Gui, D.; Zeng, F.; Liu, Z.; Zhang, B. Root characteristics of Alhagi sparsifolia seedlings in response to water supplement in an arid region, northwestern China. *J. Arid Land* **2013**, *5*, 542–551.
52. Cheng, J.; Liang, S.; Yao, Y.; Zhang, X. Estimating the optimal broadband emissivity spectral range for calculating surface longwave net radiation. *IEEE Geosci. Remote Sens. Lett.* **2013**, *10*, 401–405.
53. Peres, L.F.; DaCamara, C.C. Emissivity maps to retrieve land-surface temperature from MSG/SEVIRI. *IEEE Trans. Geosci. Remote Sens.* **2005**, *43*, 1834–1844.
54. Snyder, W.C.; Wan, Z.; Zhang, Y.; Feng, Y.Z. Classification-based emissivity for land surface temperature measurement from space. *Int. J. Remote Sens.* **1998**, *19*, 2753–2774.
55. Sun, D.; Pinker, R.T. Estimation of land surface temperature from a Geostationary Operational Environmental Satellite (GOES-8). *J. Geophys. Res.* **2003**, *108*, 4326.
56. Hulley, G.C.; Hook, S.J. The North American ASTER land surface emissivity database (NAALSED) version 2.0. *Remote Sens. Environ.* **2009**, *113*, 1967−1975.
57. Land Processes Distributed Active Archive Center. Available online: https://lpdaac.usgs.gov/products/community_products_table/ag1km (accessed on 9 August 2014).
58. Gillespie, A.; Rokugawa, S.; Matsunaga, T.; Cothern, J.S.; Hook, S.; Kahle, A.B. A temperature and emissivity separation algorithm for Advanced Spaceborne Thermal Emission and Reflection Radiometer (ASTER) images. *IEEE Trans. Geosci. Remote Sens.* **1998**, *36*, 1113–1126.
59. Tonooka, H. Accurate atmospheric correction of ASTER thermal infrared imagery using the WVS method. *IEEE Trans. Geosci. Remote Sens.* **2005**, *43*, 2778–2792.

60. Li, H.; Wang, H.; Du, Y.; Xiao, Q.; Liu, Q. *HiWATER: ASTER LST and LSE dataset in 2012 in the middle reaches of the Heihe River Basin*; Cold Arid Region Science Data Center: Lanzhou, China, 2015; doi:10.3972/hiwater.220.2015.db.
61. Wang, H.; Xiao, Q.; Li, H.; Du, Y.; Liu, Q. Investigating the impact of soil moisture on thermal infrared emissivity using ASTER data. *IEEE Geosci. Remote Sens. Lett.* **2015**, *12*, 294−298.
62. Li, Z.; Li, J.; Li, Y.; Zhang, Y.; Schmit, T.J.; Zhou, L.; Goldberg, M.D.; Menzel, W.P. Determining diurnal variations of land surface emissivity from geostationary satellites. *J. Geophys. Res.* **2012**, *117*, doi:10.1029/2012JD018279.
63. Baldridge, A.M.; Hook, S.J.; Grove, C.I.; Rivera, G. The ASTER spectral library version 2.0. *Remote Sens. Environ.* **2009**, *113*, 711–715.
64. Wan, Z.; Ng, D.; Dozier, J. Spectral emissivity measurements of land-surface materials and related radiative transfer simulations. *Adv. Space Res.* **1994**, *14*, 91−94.
65. Xu, N.; Chen, L.; Hu, X.; Zhang, L.; Zhang, P. Assessment and correction of on-orbit radiometric calibration for FY-3 VIRR thermal infrared channels. *Remote Sens.* **2014**, *6*, 2884–2897.
66. Göttsche, F.M., Hulley, G.C. Validation of six satellite-retrieved land surface emissivity products over two land cover types in a hyper-arid region. *Remote Sens. Environ.* **2012**, *124*,149−158.
67. Hulley, G.C.; Hughes, C.G.; Hook, S.J. Quantifying uncertainties in land surface temperature (LST) and emissivity retrievals from ASTER and MODIS thermal infrared data. *J. Geophys. Res.* **2012**, *117*, doi:10.1029/2012JD018506.
68. Li, S.; Yu, Y.; Sun, D.; Tarpley, D.; Zhan, X.; Chiu, L. Evaluation of 10 year AQUA/MODIS land surface temperature with SURFRAD observations. *Int. J. Remote Sens.* **2014**, *35*, 830−856.